



Location of Co and Ni promoter atoms in multi-layer MoS₂ nanocrystals for hydrotreating catalysis

Yuanyuan Zhu^a, Quentin M. Ramasse^b, Michael Brorson^a, Poul G. Moses^a, Lars P. Hansen^a, Henrik Topsøe^a, Christian F. Kisielowski^c, Stig Helveg^{a,*}

^a Haldor Topsøe A/S, Haldor Topsøes Allé 1, DK-2800, Kgs. Lyngby, Denmark

^b SuperSTEM Laboratory, STFC Daresbury, Keckwick Lane, Daresbury WA4 4AD, United Kingdom

^c Joint Center for Artificial Photosynthesis (JCAP), Lawrence Berkeley National Laboratory, 1 Cyclotron Road, Berkeley, CA 94708, USA

ARTICLE INFO

Article history:

Received 11 June 2015

Received in revised form 14 August 2015

Accepted 24 August 2015

Available online 2 October 2015

Keywords:

Heterogeneous catalysis

Hydrodesulfurization

Molybdenum disulfide

Scanning transmission electron microscopy

Electron energy loss spectroscopy

ABSTRACT

The location of Co and Ni promoter atoms in industrial-style hydrotreating catalysts is examined by combining aberration-corrected scanning transmission electron microscopy and electron energy loss spectrum imaging. The observations unambiguously demonstrate that both Co and Ni promoter atoms occupy sites at all low-indexed edge terminations of hexagonally shaped multi-layer MoS₂ nanocrystals. In contrast, similar observations for single-layer MoS₂ nanocrystals show that Co-promoter atoms preferentially attach at the (−1 0 0) S-edge termination and are absent at the (1 0 0) Mo-edge termination. The apparent discrepancy between single- and multi-layer MoS₂ nanocrystals can be explained by the 2H-MoS₂ crystal structure, for which successive MoS₂ layers alternately expose Mo- and S-edge terminations in any of the low-indexed directions. Thus, the multi-layer Co–Mo–S and Ni–Mo–S nanocrystals, formed in the present type of industrial-style hydrotreating catalyst, are consistently described as a superposition of single-layer Co–Mo–S and Ni–Mo–S structures, and in turn, provide promoted edge sites with different steric accessibility for the organic compounds in mineral oil distillates.

© 2015 Elsevier B.V. All rights reserved.

1. Introduction

In modern oil refineries, a key process is the removal of sulfur and nitrogen impurities from oil distillates by catalytic hydrotreating to alleviate the demand for clean fuels. To meet the present and future requirements on the impurity levels, more active and selective catalysts are needed. To aid the design of such improved catalysts in a rational way, intense research efforts are therefore being devoted to develop a molecular-level understanding of hydrotreating catalysis.

The industrial hydrotreating catalysts are based on nanometer-sized MoS₂ (or WS₂) particles dispersed on a high-surface area support. Although the MoS₂ nanoparticles possess hydrotreating activity, it is well known that the addition of small amounts of Co or Ni promotes the catalytic functionality. By Co- or Ni-promotion, the hydrotreating activity is known to increase overall by more than an order of magnitude and the selectivities for the hydrodesulfurization (HDS), hydrodenitrogenation (HDN) and hydrogenation (HYD) reactions are radically modified [1–6].

To establish a molecular-level understanding of the role of promoters in hydrotreating catalysis, numerous studies have focused on correlating the structure of the promoted catalysts with their catalytic functionality. From this work, the general consensus evolved that the hydrotreating activity is associated with the edges of MoS₂ nanoparticles, and that the promotion is associated with Co or Ni atoms located at the edges of MoS₂-like structures, in the so-called “Co–Mo–S” or “Ni–Mo–S” phase [7]. In fact, it has been demonstrated that the Co–Mo–S structure forms a Type I phase, consisting mainly of single-layer MoS₂ nanoparticles, and a more HDS active Type II phase, which is associated with multi-layer MoS₂ nanoparticles [3,8]. The identification of the Co–Mo–S phase was based on, e.g., Mössbauer, extended X-ray absorption fine structure and infrared spectroscopy [7,9–11]. As these spectroscopic techniques average information over volumes considerably larger than the individual nanostructures, the detailed atomic arrangement of the catalytic important edge structures of the Co–Mo–S and Ni–Mo–S phase remained unresolved for long.

Complementary real-space information of Co–Mo–S and Ni–Mo–S structures was subsequently obtained from scanning tunneling microscopy of model catalysts, consisting of Co–Mo or Ni–Mo sulfide nanoparticles prepared on a planar Au (111)

* Corresponding author.

E-mail address: sth@topsoe.dk (S. Helveg).

substrate by physical vapor deposition under ultra-high vacuum conditions, and from density functional theory calculations [12,13]. These model studies provided unprecedented new insight into the shape and edge structures of single-layer MoS₂ nanocrystals. Specifically, it was demonstrated that unpromoted MoS₂ nanocrystals obtain a triangular shape, which is terminated by the (100) Mo-edge termination. Under the same sulfiding conditions, Co and Ni stabilize more hexagonally shaped MoS₂ nanocrystals by attaching preferentially at the low-indexed (-100) S-edge termination of MoS₂ nanocrystals. The model studies also showed that Ni attaches and stabilizes a higher-indexed MoS₂ edge termination. Relating the information from the model studies to the technologically relevant catalysts is challenging because there is no guarantee that the nanostructures formed in the model studies are similar to those formed using wet impregnation, high pressure sulfidation and high-surface area supports as in the preparation of the industrial-style catalysts. Consequently, it has been a key goal to characterize the structure and chemical composition of Co–Mo–S and Ni–Mo–S phases in the industrial-style catalysts at atomic resolution.

Electron microscopy has emerged as a powerful tool for visualizing nanostructures in heterogeneous catalysts made by industrial-style procedures. In the transmission mode, electron micrographs provide a two-dimensional projected view of the three-dimensional catalyst materials. Hereby valuable information was obtained about the size, stacking and shape of MoS₂ nanocrystals [14–18]. Specifically, electron micrographs of the MoS₂ nanocrystals are beneficially obtained in the MoS₂ (001) projection, because the shape and edge terminations are thereby directly revealed. However, it is only due to recent advances that electron micrographs of MoS₂ have become available at atomic-resolution and single-atom sensitivity [19–21]. By examining industrial-style MoS₂-based catalysts, prepared using thin graphite supports, it was demonstrated that aberration-corrected high-resolution (scanning) transmission electron microscopy ((S)TEM) can unambiguously disclose information about the stacking height, shape and edge terminations of supported MoS₂ nanocrystals in the (001) projection [20,21]. Moreover, combining the STEM with concurrent electron energy-loss (EEL) spectrum imaging made it possible to show that Co atoms preferentially attach to the S-edge termination and are four-fold coordinated by S atoms in single-layer MoS₂ nanocrystals [22].

In contrast, the location of Co and Ni promoter atoms in multi-layer Co–Mo–S and Ni–Mo–S nanocrystals has not yet been resolved. It therefore remains an open issue as to whether the promoter atoms are distributed in the multi-layer nanocrystal as a simple superposition of the preferred locations identified for the single-layer nanocrystals or are attached at different edge, bulk or intercalation sites of the MoS₂ structures. In the following, this issue is addressed by combining STEM and EEL spectrum imaging of multi-layer Co–Mo–S and Ni–Mo–S nanocrystals in industrial-style hydrotreating catalysts.

2. Experimental

2.1. Catalyst and TEM sample preparation

The industrial-style Co- and Ni-promoted MoS₂ hydrotreating catalysts were prepared on a graphitic support by a sequential incipient wetness impregnation method [22]. The graphite support is generally considered as a weakly interacting support and, therefore, allows an examination of the promoter distribution inherent to the MoS₂ nanocrystals. First, a graphitic powder (Grade AO-2, Graphene Supermarket; 1400 ppm Fe) was rinsed

by excess of aqueous 1.0 mol/L oxalic acid to reduce Fe impurities to a residual content of ca. 350 ppm or below for the different preparations. Second, the rinsed powder was tabletized and granulated. The graphite granulate was then (i) impregnated with 0.023 mol/L aqueous Co (or Ni) acetate solution, (ii) dried in ambient at 383 K, (iii) impregnated with 0.070 mol/L aqueous (NH₄)₂[MoS₄] solution, (iv) transferred incipiently wet to a quartz boat, and (v) sulfided in a flow of 10% H₂S in H₂ at 1073 K for 6 h followed by cooling to room temperature before flushing with inert N₂. The nominal atomic ratio of Mo:Co (Ni) was 3:1 and the estimated Mo loading was 0.3 wt% Co (Ni) and 0.3 wt% Mo. The samples were stored and TEM samples were prepared in a dry and O₂-free atmosphere [22]. The TEM samples were prepared by crushing catalyst granulates in a mortar and by dispersing the dry powder on standard Cu TEM-grids covered with lacey carbon. The samples were only exposed to ambient conditions for a few minutes during transfer to the electron microscope.

2.2. Electron microscopy

Electron microscopy was carried out at the SuperSTEM Laboratory, Daresbury, using a Nion UltraSTEM100 dedicated aberration-corrected scanning transmission electron microscope. The instrument operates with an ultra-high base vacuum below 5×10^{-9} Torr and is equipped with a cold field emission gun with a native energy spread of 0.35 eV and the Nion quadrupole–octupole spherical-aberration corrector, with a full correction up to six-fold astigmatism. In this work, the microscope was operated at a primary beam energy of 60 keV. The probe-forming optics were configured to a beam convergence semi-angle of 30 mrad, corresponding to a probe size of ca. 0.11 nm. An estimated electron beam current of ca. 50 pA was impinging on the sample.

Aberration-corrected STEM images were acquired in the high-angle annular dark field (HAADF) mode with the detector inner and outer radii being calibrated at 85 mrad and 190 mrad, respectively. The STEM images were acquired with a dwell time of 12–36 μ s/pixel and pixel sizes of about 10^{-1} Å²/pixel, corresponding to an electron dose-rate in the order of 10^4 e[−]/Å² s and a resulting signal-to-noise ratio, S/N > 3. During part of the STEM image acquisitions, electron energy loss (EEL) spectra were concurrently recorded pixel by pixel to form the so-called EEL spectrum image. The EEL spectra were recorded using a Gatan Enfina spectrometer with a collection angle of 37 mrad, an energy dispersion of 0.7 eV/channel, enabling a parallel acquisition of the S L_{2,3}, Mo M_{4,5} and Co(Ni) L_{2,3} ionization edge spectra, and a dwell time of 50 ms/spectrum, resulting in an interpretable signal (S/N ~ 1.5) [22]. Specifically, the combined STEM-EEL spectrum imaging was conducted with a typical image pixel size of around 10^{-1} Å²/pixel and an electron dose-rate of the order of 10^6 e[−]/Å² s [22]. These electron doses for STEM-EEL spectrum image recording were about 1 to 3 orders lower than those applied in an investigation of electron beam damage of single-layer MoS₂ films [23], where it was shown that encapsulation of single-layer MoS₂ between two sheets of graphene (or to a lesser extent, the presence of one layer of graphene) lowered the damage-rate sufficiently that two-dimensional atomic-resolution EEL spectrum imaging was possible. While no encapsulation was applied in the present study, the ultra-thin graphite support may played the same protective role.

However, despite these electron illumination conditions, dynamic changes of the MoS₂ edges could still be observed during continued exposure to the electron beam. Such changes could have been due to the actual threshold for electron-induced sputtering or atom migration being lower than the theoretical value

of 66 keV for bulk MoS₂ [21]. In addition, electron and phonon excitations could also contribute to beam-induced sample changes [24]. As the relative contribution of the different damage mechanisms is poorly described in general, they were addressed by an empirical approach. That is, STEM images of a given area were recorded before and after the acquisition of an STEM-EEL spectrum image and only those regions that did not show noticeable structural changes after the final STEM image acquisition were considered for the present analysis, as also discussed in [22].

2.3. Data analysis

For analysis of the EEL spectrum images, all spectra were first denoised by principal component analysis [25] and then calibrated for any energy dispersion change or shift [22]. For generating elemental maps, the spectra were integrated over a 20 eV, 40 eV and 60 eV energy window above the edge onset of the S L_{2,3}, Mo M_{4,5} and Co(Ni) L_{2,3} ionization edges, respectively, after subtraction the decaying background using a power-law model [22]. The integrated spectrum intensities are represented as normalized, linearly colored values of an elemental map.

3. Results and discussion

Fig. 1a shows an aberration-corrected HAADF-STEM micrograph of the Co-promoted MoS₂ hydrotreating catalyst. The micrograph reflects a bright hexagonally shaped nanocrystal situated on a darker support. In the HAADF detection mode, the image intensity (*I*) is dominated by the so-called Z-contrast, which scales with the total projected atomic number (*Z*), i.e. $I \sim Z^\alpha$ ($\alpha \approx 1.7$) [26]. The image intensity (Fig. 1a) and its Fourier transform (Fig. 1b) therefore indicate that the nanocrystal is MoS₂ oriented with the (001) basal plane orthogonal to the electron beam and along the (001) plane of the graphite support. Moreover, the overall intensity across the MoS₂ basal plane has an abrupt change (Fig. 1a) indicating the presence of a step separating regions with different thickness of the MoS₂ nanocrystal. The nanocrystal thickness can be addressed by a closer inspection of the image intensity of the two contrast patches of the basal plane (Fig. 1c and d). The lower intensity patch of the MoS₂ nanocrystal reveals a dumbbell structure with intensity maxima separated by 0.18 nm along (100) and an asymmetric intensity distribution (Fig. 1c and e), which can be attributed to the pair of a 2S and 1Mo atom column of the single-layer MoS₂ basal plane (Fig. 1f) [21]. Likewise, the higher intensity patch consists of a dumbbell structure with intensity maxima separated by 0.18 nm along (100) intensity and a symmetric intensity distribution (Fig. 1d and e). In the 2H-MoS₂ unit cell, two layers of MoS₂ are translated and rotated by 60° around the *c* axis in such a way that a 2S column in one layer coincides with the 1Mo column in the next layer (Fig. 1f). Hereby, the atomic columns in a two-layer MoS₂ nanocrystal, viewed along (001), contain the same element combinations and therefore have a similar contrast. Obviously, any odd or even number of layers in a multi-layer MoS₂ nanocrystal would show up as an asymmetric or symmetric dumbbell structure in the STEM images. However, the thicker the crystal, the smaller the relative intensity difference between the atomic columns in the dumbbell becomes and such differences become successively more difficult to resolve for the present materials, especially as multi-layer nanoparticles also need to be perfectly aligned along the correct zone-axis for unambiguous contrast interpretation [21]. Thus, the image intensity analysis indicates that the nanocrystal consists of a single-layer (1L) MoS₂ that is partially covered by one or more additional MoS₂ layers in

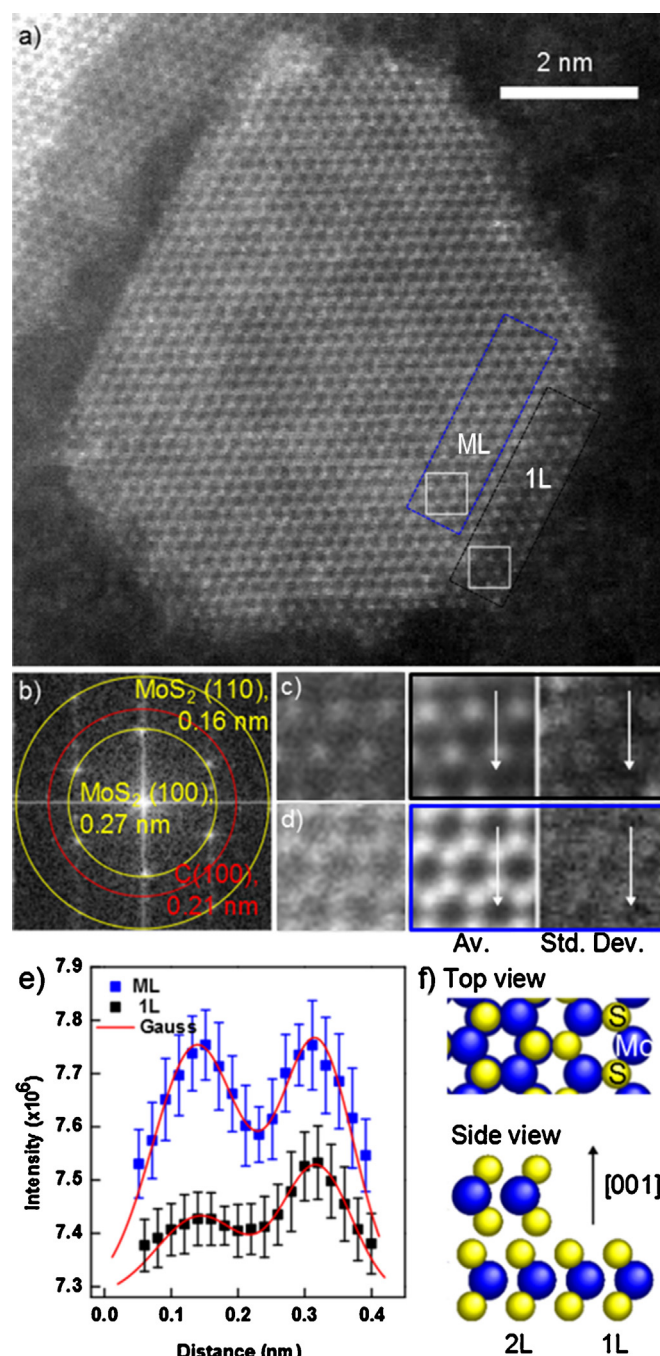


Fig. 1. (a) High-resolution STEM image of the Co-promoted MoS₂ hydrotreating catalyst showing a partial multi-layer MoS₂ nanocrystal oriented with its (001) basal plane along the (001) plane of the graphite support and orthogonal to the electron beam direction. The image is unprocessed. (b) Fourier transform of the image in (a) with an assignment of the crystal lattice vectors superimposed. (c and d) Close-up on (a) at the multi-layer (ML) and single-layer (1L) regions, indicated by white boxes in (a), and the corresponding template-average (Av.) and standard deviation (Std. Dev.) from the areas marked by blue and black boxes in (a). (e) Line-profiles of image intensities along the (-100) direction in (c) and (d). The profiles are obtained from the template-average and standard deviation images as two pixel-wide (0.04 nm) averages. The red curves represent Gaussian fits to the line-profiles obtained with fixed background intensity, corresponding to the mean intensity from the graphite support in the vicinity of the MoS₂ nanocrystal. (f) Ball models showing a top and side view of a 1L and 2L MoS₂ crystal structure (For interpretation of the references to color in this figure legend, the reader is referred to the web version of this article.).

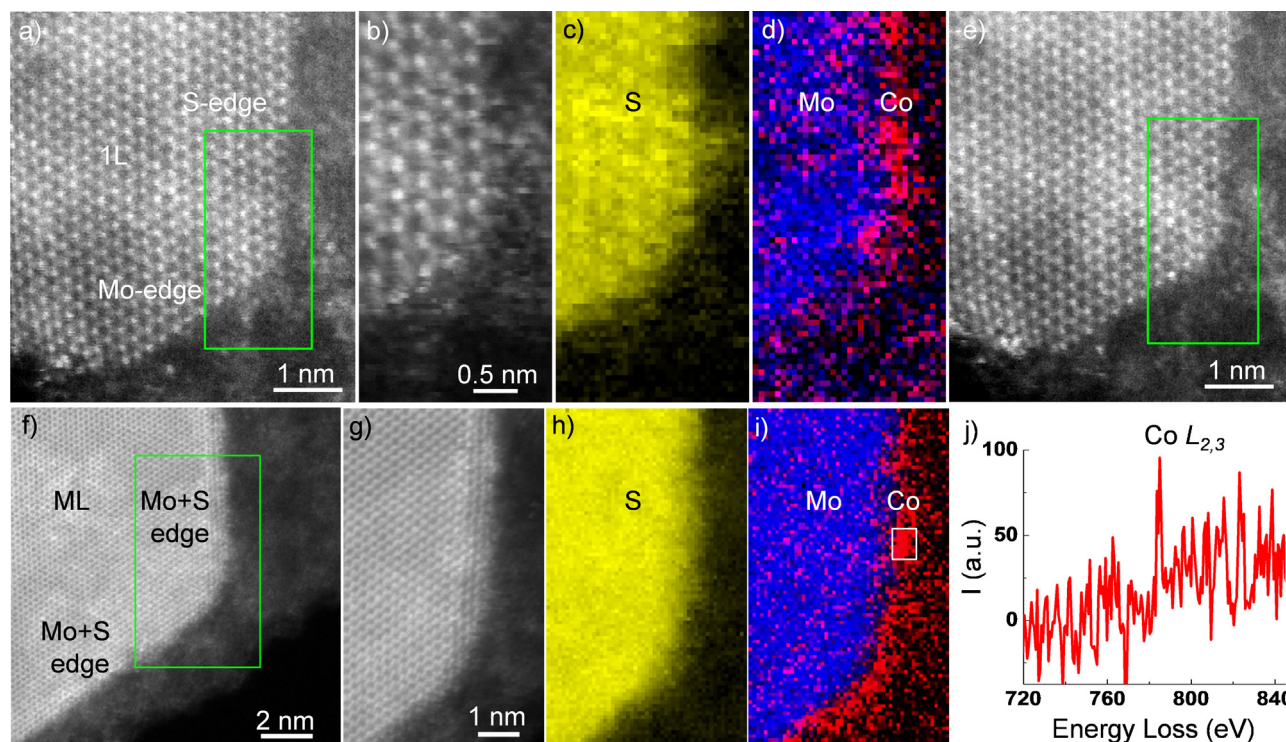


Fig. 2. (a) STEM image of a single-layer MoS₂ nanocrystal obtained prior to EEL spectrum imaging. The orientation of the asymmetric 2S-1Mo dumbbell pattern indicates the relative position of the Mo and S sub-lattices and allows the assignment of the Mo- and S-edge terminations as marked. (b) STEM image showing the framed region of (a) used for EEL spectrum imaging. (c) The corresponding element map for the S distribution. (d) The corresponding element map for the combined Mo (blue) and Co (red) distributions. (e) The STEM image of the region in (a) acquired after EEL spectrum imaging acquisition. (f) STEM image of a multi-layer MoS₂ nanocrystal obtained prior to EEL spectrum imaging. (g) STEM image showing the framed region of (a) used for EEL spectrum imaging. (h) The corresponding element map for the S distribution. (i) The corresponding element map for the combined Mo (blue) and Co (red) distributions. (j) The EEL spectrum at the Co L_{2,3} ionization edge integrated over the framed edge region in (i). The spectrum is obtained after processing the raw data as described in Section 2 (For interpretation of the references to color in this figure legend, the reader is referred to the web version of this article.).

such a way that the nanocrystal is largely a multi-layer (ML) MoS₂ nanocrystal (Fig. 1f) [20]. The low electron-dose conditions, however, imply that the detailed stoichiometry is difficult to extract based on STEM imaging only. In the following, the chemical composition of a single-layer and a multi-layer MoS₂ nanocrystal is therefore addressed by the combined STEM-EEL spectrum imaging approach.

First, the structure and composition of a single-layer Co–Mo–S nanocrystal is addressed. Fig. 2a shows a STEM image of a MoS₂ nanocrystal, which is a single-layer due to the clear asymmetric dumbbell structure of the basal plane. The dumbbell structure reflects the relative orientation of the S and Mo sub-lattices and, thus, enables an unambiguous assignment of the low-indexed (100) Mo-edge and ($\bar{1}00$) S-edge terminations (Fig. 3) [22]. Both edge terminations are present at the corner region emphasized in the close-up (Fig. 2b), from which elemental maps were obtained. Fig. 2c shows a uniform distribution of S across the basal plane with intensity maxima that coincide with the S sub-lattice in the STEM image of this single-layer nanocrystal. Fig. 2d shows the combined Mo and Co map. It demonstrates also a uniform distribution of Mo over the basal plane. The location of the Mo atoms is not clearly resolved due to the inelastic electron scattering process and lower signal-to-noise ratio of the delayed Mo M_{4,5} ionization edge in the EEL spectra [22]. Moreover, the combined Mo and Co map shows that the Co signal has an appreciable intensity confined to the S-edge and is absent in the basal plane and at the Mo-edge. This finding is inherent to the single-layer MoS₂ nanocrystals, because the STEM image obtained of the same nanocrystal after the combined STEM-EEL spectrum image acquisition confirms the integrity of the single-layer edges (Fig. 2e). Thus,

Co attaches preferentially to the S-edge on the single-layer MoS₂ nanocrystal, in agreement with [22] and with ab-initio calculations of unsupported MoS₂ slabs [27]. Moreover, Ref. [22] proposed the atomic model in Fig. 3a for the low-indexed edge terminations of the single-layer Co–Mo–S nanocrystals in the present industrial-style hydrotreating catalyst and argued that this model represents an equilibrium structure due to its insensitivity to the synthesis conditions and support material used in preparation of different model and industrial-style catalysts [12,13,22,28–31]. The preparation procedure is therefore a good starting point for an analysis of preferences in the attachment of promoter atoms to multi-layer MoS₂ nanocrystals.

Next, the location of Co promoters associated with multi-layer MoS₂ nanocrystals in the present hydrotreating catalyst is addressed. Fig. 2f shows a STEM image of a multi-layer MoS₂ nanocrystal as reflected by the approximately symmetric intensity of the dumbbell structure in the basal plane. Faint contrast variations extend over several atomic columns on the basal plane and are likely reflecting variations in the graphite support or carbon layers that partially cover the nanocrystal [22]. For comparison with the elemental distribution of the single-layer MoS₂ nanocrystals, element maps were generated at the corner emphasized in the close-up in Fig. 2g. The element maps reveal that both S and Mo are uniformly distributed across the nanocrystal (Fig. 2h and i) and that Co is located at *both* the adjacent edges (Fig. 2i). The identification of Co is based on an appreciable intensity distributed over several neighboring pixels reflecting the delocalization in the inelastic electron scattering. In contrast, individual pixels in the basal plane or on the support with an appreciable intensity are attributed to noise resulting from

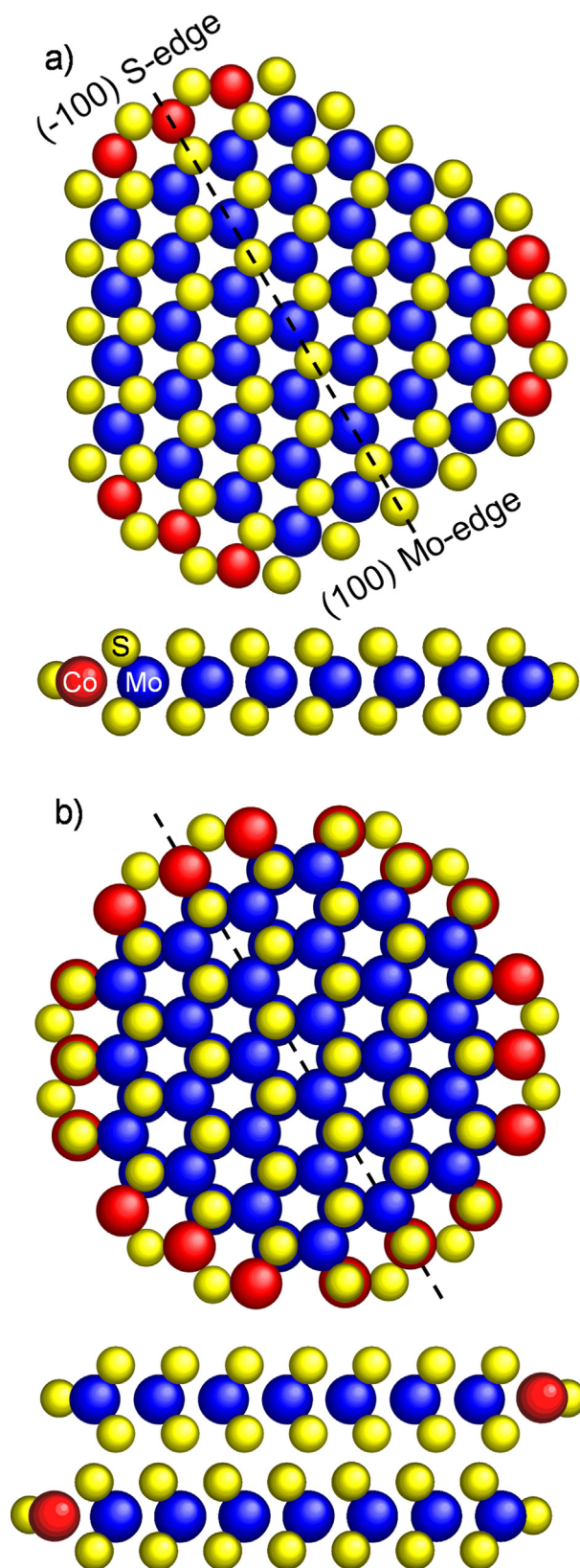


Fig. 3. (a) Ball-models for the single-layer Co-Mo-S structure in top view (upper model) and side view (lower model). Adapted from [22]. (b) Ball-models for the two-layer Co-Mo-S structure in top view (upper model) and side view (lower model). (For interpretation of the references to color in this figure legend, the reader is referred to the web version of this article.)

the rather low signal-to-noise ratio in the EEL spectra (Fig. 2j). The finding that Co attaches to *all* edge terminations on the multi-layer MoS₂ nanocrystal differs from the marked preference for attachment to the S-edge termination on single-layer MoS₂ nanocrystals. In the multi-layer nanocrystal, the edge terminations consist of alternating Mo- and S-edge terminations, respectively, exposed by the successive MoS₂ layers in the 2H-MoS₂ stacking sequence. Due to this sequence, EEL spectra obtained in the (001) projection geometry sample the composition of both Mo- and S-edge terminations, even at adjacent edges of the multi-layer MoS₂ nanocrystal. Thus, although it cannot be excluded that some Co atoms are trapped at less preferred sites at the Mo-edge termination, the observed presence of Co at all edge terminations can consistently be accounted for by the preferred attachment to the S-edge termination alone. The present multi-layer Co-Mo-S nanocrystals can therefore be explained as a simple superposition of single-layer Co-Mo-S nanocrystals, as sketched in Fig. 3b.

Finally, the Ni-promoted MoS₂ hydrotreating catalyst is examined in the same way by using combined STEM and EEL spectrum imaging. Fig. 4a shows a STEM image of two hexagonally shaped nanocrystals with an apparent partial overlap in the projected image. For nanocrystal I, a close-up on the basal plane shows a dumbbell structure with an apparent symmetric intensity (Fig. 4b) and the corresponding Fourier transform is consistent with the MoS₂ (001) structure superimposed on graphite (001) (Fig. 4c). For nanocrystal II, a more intense image signal is observed (Fig. 4d) and the corresponding Fourier transform reveals the MoS₂ structure viewed along the (001) direction (Fig. 4e). Thus, the image in Fig. 4a reflects two multi-layer MoS₂ nanocrystals with the nanocrystal I thinner than II. Moreover, in the region of partial overlap of the basal planes, a Moiré pattern is present in the STEM image (Fig. 4a) due to different rotational orientations of the nanocrystals around the electron beam direction. The perimeter of the Moiré pattern allows the deduction of the shape of nanocrystal I as a truncated hexagon and that of nanocrystal II as a regular hexagon. The overlap can be due to a geometry in which nanocrystal II partially covers nanocrystal I, in the case where the two nanocrystals are located on the same side, but on different terraces, of the graphite support. The overlap can also result from the two nanocrystals being situated on different sides of the graphite support. The projection geometry makes a clear distinction between these two configurations difficult. Across the projected area of the two nanocrystals, the element maps (Fig. 4f and g) show that S and Mo are uniformly distributed, and that a higher content of S and Mo is present in nanocrystal II than I, consistent with the thickness difference. In contrast, the element map in Fig. 4g shows that Ni is associated with a higher intensity near *all* edges of both multi-layer MoS₂ nanocrystals. Moreover, the Ni intensity is higher around the relatively thicker nanocrystal II than I, reflecting a higher projected abundance of promoters. Furthermore, the Ni promoter atoms appear to be heterogeneously distributed around the multi-layer edges (arrowheads in Fig. 4g). The wider patches with Ni seem to correlate with regions in which the successive MoS₂ layers tend to extend further, resulting in a staircase edge termination (arrowheads in Fig. 4a). Thus, these findings indicate a strong preference for Ni to attach to edges of a multi-layer MoS₂ nanocrystal in a way resembling the location of Co atoms in multi-layer Co-Mo-S nanocrystals. The single-layer MoS₂ nanocrystals in the Ni-promoted hydrotreating catalyst were not successfully resolved in the present experiments. However, the edge attachment may still be rationalized in the same way as for Co with a structural model for the multi-layer Ni-Mo-S nanocrystal as in Fig. 3b, because Ni has also been suggested to preferentially attach to the S-edge termination and not to the Mo-edge edge [13].

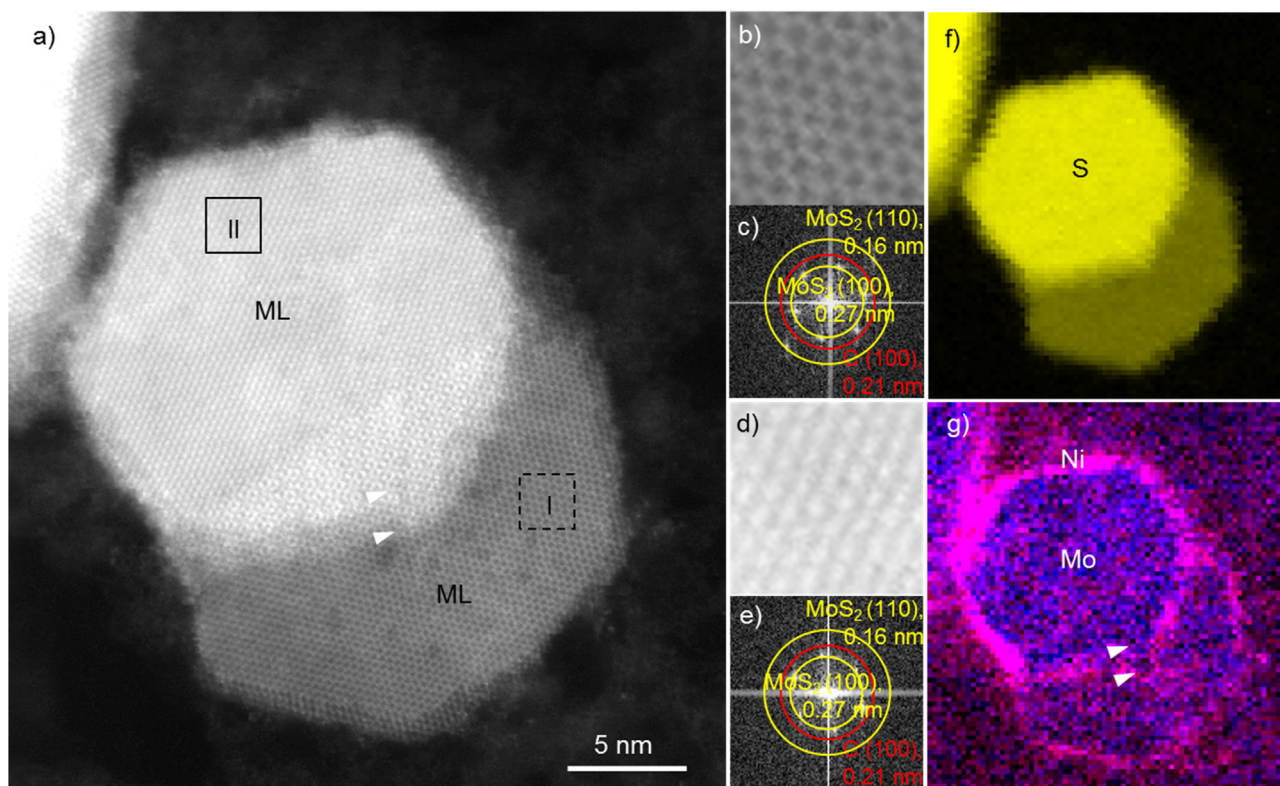


Fig. 4. (a) STEM image of two multi-layer MoS₂ nanocrystals supported by graphite. (b) Close-up (2.2 nm × 2.2 nm) on the basal plane, framed by I in (a), and (c) the corresponding Fourier transform. (d) Close-up (2.2 nm × 2.2 nm) on the basal plane, framed by II in (a), and (e) the corresponding Fourier transform. (f) The corresponding element map for the S distribution. (g) The corresponding element map for the combined Mo (blue) and Ni (red) distributions (For interpretation of the references to color in this figure legend, the reader is referred to the web version of this article.).

4. Conclusion

The promoter atoms in the present industrial-style Co–Mo–S and Ni–Mo–S hydrotreating catalysts are unambiguously demonstrated to occupy sites at all <100> edge terminations of hexagonally shaped multi-layer MoS₂ nanocrystals. In contrast, for single-layer MoS₂ nanocrystals, Co-promoter atoms are found to attach preferentially at the S-edge termination and to be absent at the Mo-edge termination. This apparent discrepancy between single- and multi-layer MoS₂ nanocrystals is explained by the 2H stacking sequence of the MoS₂ nanocrystals that successively expose alternating Mo- and S-edge terminations in any of the low-indexed directions. Thus, for the present catalysts, the multi-layer Co–Mo–S and Ni–Mo–S nanocrystals are described as a superposition of single-layer Co–Mo–S and Ni–Mo–S structures with the promoter atoms located at the S-edge terminations at the extended edges. The different layers in multi-layer MoS₂ nanocrystals have previously been proposed to provide different catalytic functionality [32]. Thus, the present findings suggest that the promoter atoms may contribute with different effects in hydrotreating catalysis. That is, the promoted edge sites in the uppermost MoS₂ layer have full gas-accessibility and can therefore be expected to provide optimal hydrogenation properties and selectivity for the desulfurization pathways. In contrast, promoted sites associated with lower-lying MoS₂ layers may be expected to function subject to a higher degree of steric hindrance for the adsorption. Furthermore, the similarity of the Co and Ni promoted structures proposed in the present study suggests that different reactivity induced by the promoter atoms are likely due to electronic effects. Thus, the present study should be a good starting point for addressing the effect of promoters on the properties of multi-layer MoS₂ hydrotreating catalysts.

Acknowledgements

The electron microscopy was performed at the SuperSTEM Laboratory, Daresbury, and supported by the EPSRC (UK). The Danish Council for Strategic Research (grant Cat-C) and the Danish Council for Independent Research (grant HYDECAT, DFF-1335-00016) are gratefully acknowledged for financial support. C.F.K. acknowledges the Joint Center for Artificial Photosynthesis, a DOE Energy Innovation Hub, supported through the Office of Science of the US Department of Energy (DE-SC0004993).

References

- [1] X. Li, A. Wang, M. Egorova, R. Prins, *J. Catal.* 250 (2007) 283.
- [2] P. Raybaud, H. Toulhoat, *Catalysis by Transition Metal Sulphides. From Molecular Theory to Industrial Application*, Technip, Paris, 2013.
- [3] H. Topsøe, B.S. Clausen, F. Massoth, in: J.R. Anderson, M. Boudart (Eds.), *Catalysis – Science and Technology*, vol. 11, Springer, Berlin, 1996, pp. 1–310.
- [4] P.G. Moses, L. Grabow, E. Fernandez, B. Hinnemann, H. Topsøe, K. Knudsen, J.K. Nørskov, *Catal. Lett.* 144 (2014) 1425.
- [5] J. Kibsgaard, A. Tuxen, K.G. Knudsen, M. Brorson, H. Topsøe, E. Lægsgaard, J.V. Lauritsen, F. Besenbacher, *J. Catal.* 272 (2010) 195.
- [6] E. Krebs, B. Silvi, A. Daudin, P. Raybaud, *J. Catal.* 260 (2008) 276.
- [7] H. Topsøe, B.S. Clausen, R. Candia, C. Wivel, S. Mørup, *J. Catal.* 68 (1981) 433.
- [8] R. Candia, O. Sørensen, J. Villadsen, N.Y. Topsøe, B.S. Clausen, H. Topsøe, *Bull. Soc. Chim. Belg.* 93 (1984) 763.
- [9] C. Wivel, R. Candia, B.S. Clausen, S. Mørup, H. Topsøe, *J. Catal.* 68 (1981) 453.
- [10] N. Topsøe, *J. Catal.* 84 (1983) 386.
- [11] B.S. Clausen, H. Topsøe, R. Candia, J. Villadsen, B. Lengeler, J. Als-Nielsen, F. Christensen, *J. Phys. Chem.* 85 (1981) 3868.
- [12] J.V. Lauritsen, S. Helveg, E. Lægsgaard, I. Stensgaard, B. Clausen, H. Topsøe, F. Besenbacher, *J. Catal.* 197 (2001) 1.
- [13] J.V. Lauritsen, J. Kibsgaard, G.H. Olesen, P.G. Moses, B. Hinnemann, S. Helveg, J.K. Nørskov, B.S. Clausen, H. Topsøe, E. Lægsgaard, F. Besenbacher, *J. Catal.* 249 (2007) 220.
- [14] K.P. de Jong, L.C.A. van der Oetelaar, E.T.C. Vogt, S. Eijbouts, A.J. Koster, H. Friedrich, P.E. de Jongh, *J. Phys. Chem. B* 110 (2006) 10209.

- [15] E.J.M. Hensen, P.J. Kooyman, Y. van der Meer, A.M. van der Kraan, V.H.J. de Beer, J.A.R. van Veen, R.A. van Santen, *J. Catal.* 199 (2001) 224.
- [16] R.M. Stockman, H.W. Zandbergen, A.D. van Langeveld, J.A. Moulijn, *J. Mol. Catal. A* 102 (1995) 147.
- [17] O. Sørensen, B.S. Clausen, R. Candia, H. Topsøe, *Appl. Catal.* 13 (1985) 363.
- [18] M. Brorson, A. Carlsson, H. Topsøe, *Catal. Today* 123 (2007) 31.
- [19] F.L. Deepak, R. Esparza, B. Borges, X. Lopez-Lozano, M. Jose-Yacaman, *ACS Catal.* 1 (2001) 537.
- [20] C. Kisielowski, Q.M. Ramasse, L.P. Hansen, M. Brorson, A. Carlsson, A.M. Molenbroek, H. Topsøe, S. Helveg, *Angew. Chem. Int. Ed.* 49 (2010) 2708.
- [21] L.P. Hansen, Q.M. Ramasse, C. Kisielowski, M. Brorson, E. Johnson, H. Topsøe, S. Helveg, *Angew. Chem. Int. Ed.* 50 (2011) 10153.
- [22] Y. Zhu, Q.M. Ramasse, M. Brorson, P.G. Moses, L.P. Hansen, C.F. Kisielowski, S. Helveg, *Angew. Chem. Int. Ed.* 53 (2014) 10723.
- [23] R. Zan, Q.M. Ramasse, R. Jilil, T. Georgiou, U. Bangert, K.S. Novoselov, *ACS Nano* 7 (2013) 10167.
- [24] C. Kisielowski, L.-W. Wang, P. Specht, H.A. Calderon, B. Barton, B. Jiang, J.H. Kang, R. Cieslinski, *Phys. Rev. B* 88 (2013) 024305.
- [25] N. Bonnet, N. Brun, C. Colliex, *Ultramicroscopy* 77 (1999) 97.
- [26] P. Hartel, H. Rose, C. Dinges, *Ultramicroscopy* 63 (1996) 93.
- [27] L. Byskov, J.K. Nørskov, B.S. Clausen, H. Topsøe, *J. Catal.* 187 (1999) 109.
- [28] B.S. Clausen, B. Lengeler, R. Candia, J. Als-Nielsen, H. Topsøe, *Bull. Soc. Chim. Belg.* 90 (1981) 1249.
- [29] S.M.A.M. Bouwens, J.A.R. van Veen, D.C. Koningsberger, V.H.J. de Beer, R. Prins, *J. Phys. Chem.* 95 (1991) 123.
- [30] P.G. Moses, B. Hinnemann, H. Topsøe, J.K. Nørskov, *J. Catal.* 268 (2009) 201.
- [31] H. Schweiger, P. Raybaud, H. Toulhoat, *J. Catal.* 212 (2002) 33.
- [32] M. Daage, R.R. Chianelli, *J. Catal.* 149 (1994) 414.